

BINARY COLLISION OF BURNING AND NON-BURNING DROPLETS OF XYLENE

BY

RAHUL NITIN GANDHI

A thesis submitted to the

Graduate School—New Brunswick

Rutgers, The State University of New Jersey

in partial fulfillment of the requirements

for the degree of

Master of Science

Graduate Program in Mechanical and Aerospace Engineering

Written under the direction of

Prof. Stephen Tse

and approved by

New Brunswick, New Jersey

October, 2017

ABSTRACT OF THE THESIS

Binary Collision of Burning and Non-Burning Droplets of Xylene

by Rahul Nitin Gandhi

Thesis Director: Prof. Stephen Tse

The collision behavior of a burning droplet of xylene with a non-burning droplet of xylene is studied. Two piezoelectric droplet generators are used to generate streams of isolated mono-dispersed droplets. These droplet generators are placed vertically opposite to each-other, and the droplets are generated at a frequency of 6 Hz. Droplet diameters range from $80\mu m$ to $95\mu m$; and droplet velocities vary from $0.7m/s - 1.5m/s$, for the lower droplet and from $1.5m/s - 2.5m/s$, for the upper droplet. The droplet streams are confined within a cuvette. The collision occurs at atmospheric pressure, and a constant supply of O_2 is maintained in the cuvette to allow burning of the droplet. A CCD strobe is used to detect the two droplets and make adjustments to have them collide. The lower droplet is ignited with a spark. For the experiments, the collision process is recorded using a high-speed camera. The relative velocity and impact parameter of the collisions are varied by changing the supply current to the piezoelectric droplet generators and by moving the lower droplet, respectively. The recorded videos of the collision process are analyzed using a MATLAB script to track the droplets and calculate their velocities and the impact parameter in each case. The collision outcomes are studied under a range of Weber numbers and for varying Impact Parameter. The post-collision behavior of the xylene flame suggests that the gas between the colliding

droplets is rapidly ejected, and the flow pattern greatly affects the progression of the flame. With the introduction of a burning droplet, existing theoretical models may need to be refined to better predict the onset of various collision regimes.

Acknowledgements

First and foremost, I would like to thank my advisor, Professor Stephen D. Tse, for giving me the opportunity to work on this project, and for his patience and support throughout the course of this work. This project would not have been successful without his constant enthusiasm and encouragement. I would also like to thank Professor German Drazer and Professor Aaron Mazzeo for taking the time out of their schedules to be on the thesis review committee. The financial support from the Army Research Office (grants W911NF-14-1-0412 and W911NF-16-1-0015) is gratefully acknowledged.

I would, sincerely, like to thank Dr. Gang Xiong for his tremendous help throughout the project, helping me with the experimental setup, and for sharing his insights on the project. I would also like to thank Ph.D. candidate Xiaosheng Zhong for his help with designing the experimental setup and helping me run the experiments. I wish him success with his endeavors here, at Rutgers. I greatly appreciate their support to accommodate my eccentric lab hours.

Most importantly, I would like to thank my family and friends who have been through all the ups and downs and encouraged me to keep on moving forward.

Dedication

Dedicated to my family, Utpala Gandhi, Nitin Gandhi and Karan Gandhi

Without whose support my work would not have been possible.

Table of Contents

Abstract	ii
Acknowledgements	iv
Dedication	v
List of Tables	viii
List of Figures	ix
1. Introduction	1
1.1. Objective	1
1.2. Background	1
1.3. Literature Review	6
1.4. Droplet Combustion	8
1.5. Thesis Outline	10
2. Theory	11
2.1. Theoretical description of reflexive separation and models for the bound- ary curve between coalescence and reflexive separation	11
2.2. Theoretical description of stretching separation and models for the bound- ary curve between coalescence and stretching separation	13
3. Experimental Design	16
3.1. Droplet generation and Ignition	16
3.2. Image acquisition system	19
3.3. Image Processing	21
3.4. Experimental procedure	21

3.5. Working fluid and thermo-physical properties	23
4. Results and discussions	25
4.1. Image processing and droplet tracking	25
4.2. Droplet and flame evolution for various collision regimes	26
4.2.1. Head-on or nearly head-on collisions	28
4.2.2. Off-center collisions	29
4.3. Comparison of experimental data with analytical models	38
5. Conclusion and future scope	40
References	41

List of Tables

3.1. Properties of m-xylene at $T = 412K$	23
---	----

List of Figures

1.1. Calculating the Impact parameter from recorded images	3
1.2. A typical collision map for water (1.2a) and hydrocarbon (1.2b) droplets based on We number and impact parameter. Figure adapted from Qian & Law [1]	5
1.3. Time shifted evolution of the droplet and flame diameters, for three xylene droplets with different ignition points, at 0.4 L/min co-flowing oxygen. Figure adapted from Rosebrock <i>et al.</i> [2]	9
1.4. Time shifted evolution of droplet velocity, for three xylene droplets with different ignition points, at 0.4 L/min co-flowing oxygen. Figure adapted from Rosebrock <i>et al.</i> [2]	10
2.1. Boundary curves between coalescence and reflexive separation. $Ca = 0.06$	13
2.2. Boundary curves between coalescence and stretching separation. $Ca =$ $Oh\sqrt{We}$	15
3.1. Experimental setup showing the layout of the droplet generators from the point of view of the high-speed camera [2]	17
3.2. LabVIEW interface for controlling the signal sent to the droplet genera- tors, LED strobe and ignition system.	18
3.3. Layout of the optical system to record high-speed images	20
4.1. Comparison of the raw image with the post-processed image. The blue and green circles are the circles detected by MATLAB.	26
4.2. Flame structure of a xylene droplet burning in Oxygen coflowing at 0.4 L/min. Image recorded by Rosebrock <i>et al.</i> [2]	27
4.3. Formation of vortex rings and pressure distribution. Image by Nikolopou- los <i>et al.</i> [3]	29

4.4.	Collision images from the high-speed camera. The smaller burning droplet is moving from right to left while the larger droplet is moving from left to right	30
4.4.	Collision images from the high-speed camera. The smaller burning droplet is moving from right to left while the larger droplet is moving from left to right	31
4.4.	Collision images from the high-speed camera. The smaller burning droplet is moving from right to left while the larger droplet is moving from left to right	32
4.5.	Formation of vortices around the gas jet squeezed out during collision. R_o is the initial droplet radius. Image by Nikolopoulos <i>et al.</i> [4]	33
4.5.	Collision images from the high-speed camera. The smaller burning droplet is moving from right to left while the larger droplet is moving from left to right	34
4.5.	Collision images from the high-speed camera. The smaller burning droplet is moving from right to left while the larger droplet is moving from left to right	35
4.6.	Formation of vortices around the gas jet squeezed out during stretching separation at low impact parameters. R_o is the initial droplet radius. Image by Nikolopoulos <i>et al.</i> [4]	36
4.7.	Formation of vortices around the connecting ligament during stretching separation at low impact parameters. R_o is the initial droplet radius. Image by Nikolopoulos <i>et al.</i> [4]	37
4.8.	Experimental data compared to phenomenological boundary curves . . .	38

Chapter 1

Introduction

1.1 Objective

Collision outcomes of binary liquid droplets can be affected by various parameters such as droplet diameters, ambient atmosphere and pressure, droplet kinetic energy, collision impact parameter, and properties of the fluids. Collision behavior of hydrocarbon droplets have been widely studied since the latter half of the 20th century because of their importance in designing fuel sprays. However, the reported studies on the collision behavior of *burning* hydrocarbon droplets are limited.

The objective of this thesis is to present the collision outcomes of a burning droplet colliding with a non-burning droplet of Xylene. Collisions are recorded by a high-speed camera under different values of the collision Weber number and impact parameter. The regimes of post-collision outcomes are compared to other works in literature pertaining mainly to the collision of non-burning droplets.

1.2 Background

Binary collision of liquid droplets has been studied for a span of decades. Initially the primary interest was to understand meteorological phenomenon such as the formation of atmospheric raindrops and related pollution behavior. Thus, earlier studies employed water droplets colliding at atmospheric pressure (Adam *et al.* [5], Brazier smith *et al.* [6], Ashgriz & Poo [7]). More recently, post collision behavior of hydrocarbon droplets has been of growing importance, primarily for the applications to spray combustion systems. Since the rheological properties of hydrocarbons are usually very different from those of water, there have been experimental studies on the collision behavior of hydrocarbon

droplets at atmospheric conditions (Jiang *et al.* [8] , Estrade *et al.* [9], M Orme [10], Chen *et al.* [11], Gao *et al.* [12]) as well as different pressures and gas phases (Qian & Law [1], Willis & Orme [13]).

All the studies mentioned above have been carried out in the absence combustion. Ashgriz & Givi ([14] & [15]), conducted experiments on collision of both the burning and non-burning droplets of n-hexane. However, this study was limited to a very small range of collision Weber number, and the collision impact parameter was not explicitly mentioned.

For a proper understanding of droplet collisions, all the involved physical properties, as well as geometrical properties of the collision system, need to be considered. The physical properties are viscosity, density, and surface tension whereas the geometrical properties are the droplet diameter, velocity, and the collision impact parameter. To simplify the problem and to reduce the number of variables to be studied, certain dimensionless parameters are used. The dimensionless number used depends on the objective of the study. Brazier-Smith *et al.* [6] introduced the most important parameter used, the Weber number (We), which is the ratio of the inertial force of the droplets to the surface tension force. The parameters of interest in this study are the collision Weber number (We) and the impact parameter (B), where We and impact parameter B are defined as $2R_s\rho U^2/\sigma$ and $\chi/(R_s+R_l)$ respectively. R_s and R_l represent the radius of the smaller droplet and the larger droplet respectively. ρ and σ are the density and surface tension of the liquid respectively. U is the relative velocity and χ is defined as the distance between the center of one droplet to the relative velocity vector placed at the center of the second droplet. Thus, the value of B ranges from 0 to 1 where $B = 0$ indicates head-on collision and $B = 1$ indicates grazing collision. Here, U is calculated using the cosine law,

$$U = \sqrt{V_1^2 + V_2^2 - 2V_1V_2\cos(\theta_1 + \theta_2)}$$

and,

$$\chi = d \sin(\psi)$$

where d is the distance between the two centers.

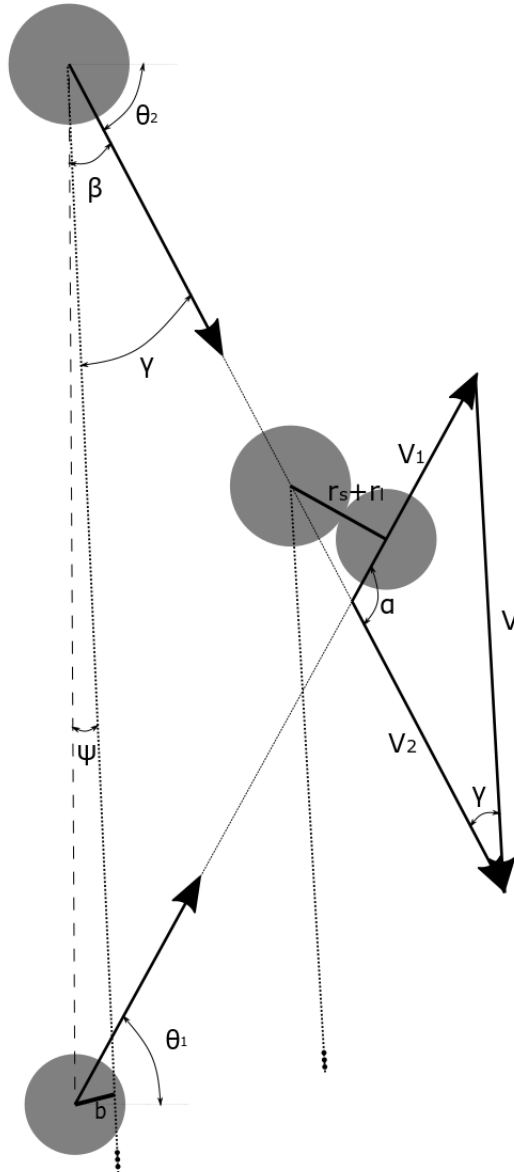


Figure 1.1: Calculating the Impact parameter from recorded images

From figure 1.1, γ can be calculated as:

$$\frac{\sin \alpha}{V} = \frac{\sin \gamma}{V_1}$$

where, $\alpha = \theta_1 + \theta_2$. The angle ψ can then be calculate as $(\beta - \gamma)$, where, β is the angle between the droplet trajectory and the line connecting the two droplets.

The different post-collision regimes can be graphically represented by plotting the impact parameter against the We number. Other non-dimensional parameters used for droplet collision studies are the Ohnesorge number (Oh) and the Capillary number (Ca), where,

$$Oh = \frac{\mu}{\sqrt{\sigma \rho D_s}}$$

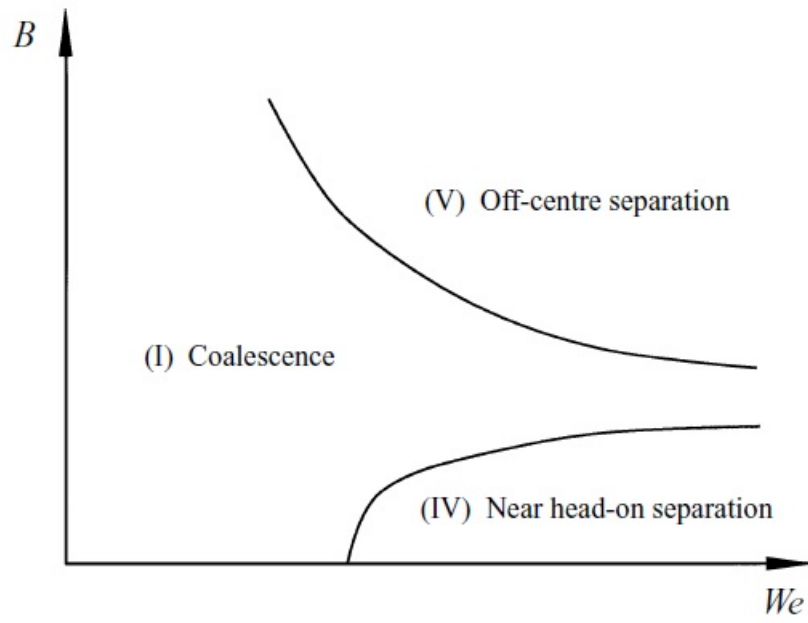
and

$$Ca = Oh\sqrt{We}$$

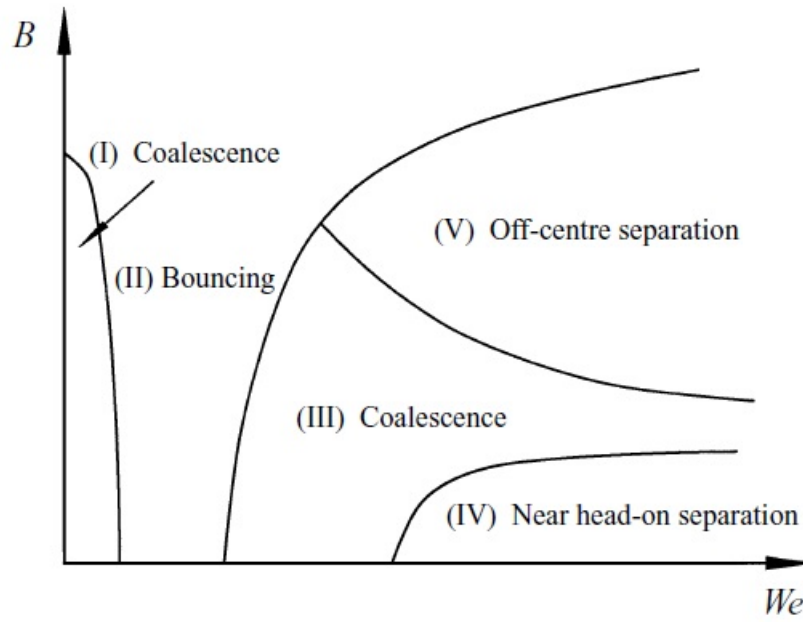
These parameters are mainly used to study the effects of viscosity on collision outcomes.

According to most papers mentioned above, there exist five distinct collision regimes for binary droplet collisions i.e., **(I)** coalescence with minor deformation, **(II)** bouncing, **(III)** coalescence with major deformation, **(IV)** near head on or reflexive separation, and **(V)** stretching separation. Figure 1.2a and figure 1.2b represent the typical post-collision regimes for water droplets and hydrocarbon droplets, respectively. These figures make it apparent that the collision dynamics for hydrocarbon droplets are significantly different and far diverse than that for water droplets. For water droplets, Figure 1.2a shows that droplets coalesce permanently **(I)** to form a single droplet for low Weber number collisions. Once the collision Weber number reaches a sufficiently high critical value, the coalescence is only temporary and the droplets break apart eventually.

In these situations, the characteristics of the break up depend upon the impact parameter. For head on collisions, the post-collision mass gets spread and forms a flat disk. The fluid at the edge of this disc reflexes back towards the center because of the surface tension forces acting on it, and the liquid contracts to form a vertical disk. For Weber numbers above the critical value, this disk eventually disintegrates and, in some cases, forms one or more satellite droplets. Hence, the term reflexive separation **(IV)**. Alternatively, for higher values of impact parameter, the collision results in stretching separation. For high impact parameter collisions, there is a competition between the



(a)



(b)

Figure 1.2: A typical collision map for water (1.2a) and hydrocarbon (1.2b) droplets based on We number and impact parameter. Figure adapted from Qian & Law [1]

surface tension force due to the interacting portions of the two droplets, and the collision kinetic energy of the non-interacting regions of the droplets. Surface tension tries to hold the droplet together while the kinetic energy of the non-interacting region forces the droplets to continue along their original trajectories. For Weber numbers over the critical value, the kinetic energy overcomes the surface tension forces and results in the stretching separation **(IV)** with the formation of one or more satellite droplets. For a fixed Weber number, an increase in the impact parameter results in an increase in the number of satellite droplets formed.

As seen in figure 1.2b, in the case of collision of hydrocarbon droplets, coalescence does not occur for all Weber numbers. Once the Weber number increases beyond a critical value, the droplets bounce off without merging initially **(II)**. This phenomenon occurs due to the presence of a thin gas film between the two droplet surfaces. The droplets will fail to coalesce if the kinetic energy of the collision is unable to expel this gas film. In such a case, the droplets will undergo deformation but will not make contact. MacKay & Mason [16] have deduced (and it has been widely accepted) that the critical gas film thickness to achieve coalescence is 10 *nm*. For extremely low Weber number cases, the droplet velocities are low enough to allow the intervening gas film enough time to escape the region, and thus the two liquid surfaces touch and coalesce. Beyond a certain Weber number, the velocities of the droplets are high such that the collisional kinetic energy is high enough to rupture the gas film.

1.3 Literature Review

A large number of experimental work has been devoted to the study of binary droplet collision. Beginning in the 1960s, raindrop growth was the primary focus of the studies on droplet collision. (Schotland 1960 [17], Jayaratne and Mason 1964 [18]) Following these studies, it was concluded that the collision outcome depends on the collision Weber number (We) and the impact parameter (B). Braizer-smith *et al.* [6] were the first to introduce the droplet diameter ratio (Δ), while studying the collision of water droplets. Their aim was to determine the parameters when bouncing occurs. Based on We , B and (Δ), they proposed a curve between regimes **(III)** and **(V)** and introduced

the concept of coalescence efficiency, which is the fraction of colliding droplets that coalesce. They also proposed a curve between regimes **(II)** and **(III)**, but this was not corroborated with experimental data.

Ashgriz & Givi (87 [14] & 89 [15]) presented the only study of binary collision of burning droplets. However, their studies were limited to very low weber numbers. They observed that droplet bounce did not occur in their cases of burning droplets, as compared to collisions between non-burning droplets for the same Weber numbers.

Ashgriz & Poo (1990) [7], Jiang *et al.* (1992) [8] and Qian & Law (1997) [1] started presenting collision data on WeB plots and thus established the distinct collision regimes. Poo studied collisions at different diameter ratios and for weber numbers ranging from 0 – 100. They proposed theoretical models to derive the curves between regimes **(III)** & **(V)** and regimes **(III)** & **(IV)**, taking into consideration Δ . This work was further extended by Jiang *et al.* (92) [8], and they proposed the only theoretical model where the effects of viscosity have been included. Their study showed that the critical Weber number for the onset of reflexive separation increases as the ratio of the liquids viscosity to its surface tension increases. Qian & Law (97) [1] gave experimental results showing the effects of viscosity by using the Ohnesorge number (Oh). Their work demonstrated the linear evolution of the curve between regimes **(III)** & **(IV)** with respect to Oh . They also studied the effects of pressure and molecular weight of the surrounding gas, along with the concentration of hydrocarbon vapor surrounding the droplets, on droplet evolution. It was demonstrated that the presence of hydrocarbon vapor in the surrounding gases increases the coalescence efficiency. To get a better understanding of the effects of viscosity on the evolution of the post collision droplet, Willis & Orme (2003) [13] conducted experiments in vacuum. They concluded that energy dissipation depends on the droplet viscosity. This conclusion contradicted the assumptions made by Jiang *et al.* [8] and showed that their models are only valid for collision of liquids with a low viscosity such as water.

Brenn *et al.* [19] performed experiments with propanol to study the formation of satellite droplets after stretching separation. They showed that the length and time taken to break the ligament connecting two droplets increases with We and decreases

as B increases. They proposed a model for stretching separation which included the effects of viscosity but the model did not agree with experimental data for low viscosity liquids such as water.

Gao *et al.* [12] performed droplet collision experiments using two miscible fluids with very different surface tensions, using water and ethanol. Their investigation showed that at higher impact parameters, for regimes of coalescence and stretching separation, the behavior follows that of the liquid with the lower surface tension. For lower impact parameter collisions, a large deformation on the droplet with the higher surface tension was observed, sometimes resulting in the formation of small satellite droplets. This phenomenon was termed as an unbalanced-surface-force (USF) deformation.

A wide range of viscosities was studied both experimentally and numerically by Gotaas *et al.* [20]. They developed a model for the boundary between coalescence and stretching separation and concluded that it shifts to higher We as viscosity increases. Recently, a comprehensive analysis of all the empirical curves proposed and the experimental data supporting these curves was carried out by Krishnan & Loth [21]. They used the experimental data available in literature to study the effects of droplet viscosity and properties of surrounding gas. It was concluded that though the inviscid dynamics of droplet collision play a major role at high We , secondary effects cannot be neglected, as was assumed in earlier works. Two revised models were proposed for the boundary between reflexive separation and coalescence and the boundary between coalescence and stretching separation.

1.4 Droplet Combustion

The experiment setup used here is the same as the one used by Rosebrock *et al.* [2]. They studied the burning of a single droplet of xylene, for which the same parametric conditions are used in the current work. Thus, their results can be directly applied here. They have shown that the burning behavior of the droplet remains the same regardless of, their distance from the spark during ignition, and the initial droplet momentum (voltage impulse). Figure 1.3 shows that the ratio of droplet and flame diameter remain

constant regardless of the ignition point. Figure 1.4 shows that the droplet velocity does change in such a case, but since we calculate the velocity individually for each collision event, this is not unacceptable for the current work. It has also been noted that xylene has a high sooting tendency because of its benzene ring and this can decrease reaction rates and therefore lead to accumulation of fuel vapor between the droplet and the flame.

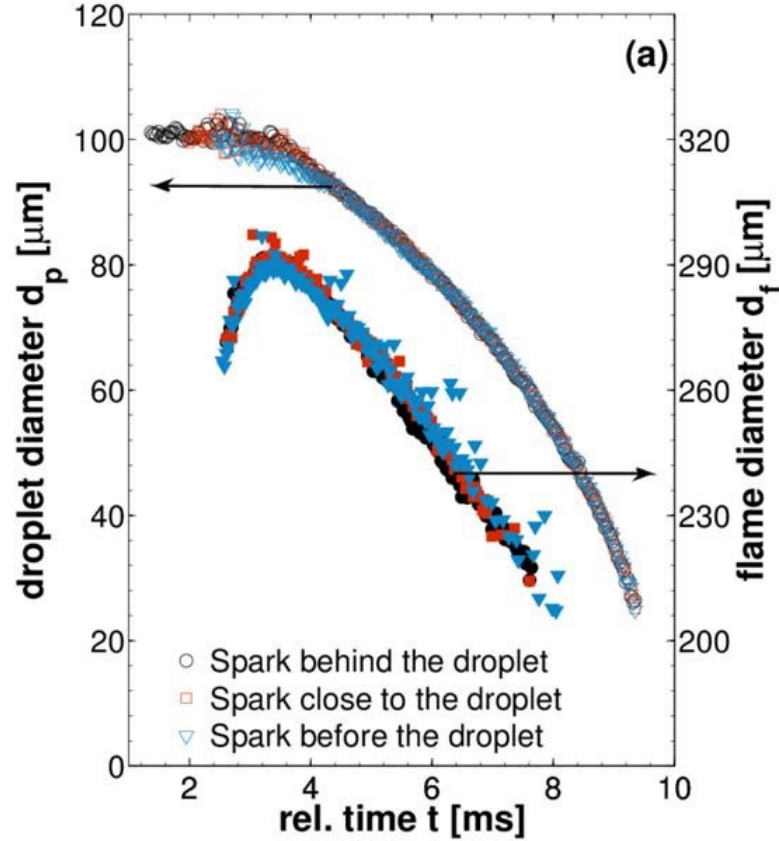


Figure 1.3: Time shifted evolution of the droplet and flame diameters, for three xylene droplets with different ignition points, at 0.4 L/min co-flowing oxygen. Figure adapted from Rosebrock *et al.* [2]

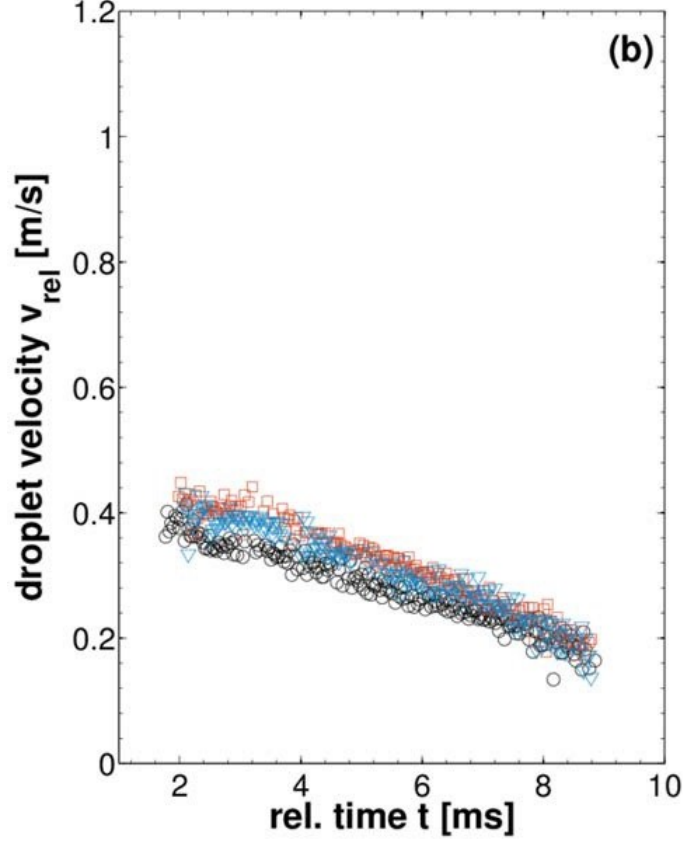


Figure 1.4: Time shifted evolution of droplet velocity, for three xylene droplets with different ignition points, at 0.4 L/min co-flowing oxygen. Figure adapted from Rosebrock *et al.* [2]

1.5 Thesis Outline

The thesis consists of 5 chapters of which the first chapter is the introductory chapter. Chapter 2 presents some of the phenomenological models proposed in literature, and the theory behind them, that are applicable for the current work. Chapter 3 describes in detail the experimental setup and the procedure carried out to obtain the data. Chapter 4 discusses the observations derived from the experiments and compares the experimental data with existing theoretical models. Chapter 5 concludes the thesis and discusses the future scope for this study.

Chapter 2

Theory

This chapter details the existing theoretical and phenomenological models proposed to describe experimental observations of the various collision types. As mentioned above, several non-dimensional numbers are used to describe the post collision behavior of binary droplets. Figure 1.2b identifies the different regimes of post collision outcomes by plotting the collision weber number against the impact parameter. Many studies have performed energy balance analysis to determine the collision boundaries. The primary difference between these studies has been the consideration of the effects of viscosity and, in particular, the effects of viscous dissipation on collision outcomes.

2.1 Theoretical description of reflexive separation and models for the boundary curve between coalescence and reflexive separation

Ashgriz & Poo [7] proposed a model to predict the boundary between coalescence and reflexive separation for low viscosity fluids. The model is based on the energy balance between the incoming kinetic energy of the moving droplets and the total surface tension of the cylinder formed caused by the reflexive action. The model proposes that if the kinetic energy is more than 75% of the total surface energy of the resulting fluid volume, the coalesced mass will stretch and separate to form multiple droplets. The model also takes into consideration the droplet diameter ratios (Δ). The equation for the boundary curve is:

$$\frac{We}{\Delta(1 + \Delta^3)^2}(\Delta^6\eta_1 + \eta_2) + 3[4(1 + \Delta^2) - 7(1 + \Delta^3)^{\frac{2}{3}}] = 0, \quad (2.1)$$

where, η_1 and η_2 are defined as,

$$\eta_1 = 2(1 - \zeta)^2(1 - \zeta^2)^{\frac{1}{2}} - 1, \quad (2.2)$$

$$\eta_2 = 2(\Delta - \zeta)^2(\Delta - \zeta^2)^{\frac{1}{2}} - \Delta^3, \quad (2.3)$$

and ζ is expressed as,

$$\zeta = \frac{B(1 + \Delta)}{2}. \quad (2.4)$$

This model assumes that none of the kinetic energy or the surface energy is lost because of viscous flows within the liquid droplet. Qian & Law [1] attempted to include this effect by proposing a relation to calculate We_c which is the critical weber number at $B = 0$ where reflexive separation first occurs.

$$We_c = C_1 Oh + C_2, \quad (2.5)$$

where, C_1 and C_2 are constants.

Jiang *et al.* and also Qian & Law assumed that the viscous dissipation is constant and does not depend on the viscosity of the droplet fluid. This was proved to be incorrect by Willis & Orme [13] by conducting experiments in vacuum using different fluids with very different viscosities. Viscous loss predominantly occurs in the period between the instance of head-on collision resulting in the formation of a disk and the consequent reflexive action leading to the formation of a cylindrical column of the fluid. Finotello *et al.* [22] proposed a model which was based on Poos model, where they assume that separation occurs if the reflexive energy is more than 75% of the post collision surface energy, while taking into account that a fraction, f , of the reflexive energy is lost because of viscous dissipation. The value of the fraction f depends on the capillary number (Ca) and is defined empirically as,

$$f = \frac{5Ca}{1 + 5Ca}. \quad (2.6)$$

and the curve is given by,

$$We = \frac{12\Delta(1 + \Delta^3)^2}{\Delta^6\eta_1 + \eta_2} \frac{[(1.75 - f)(1 + \Delta^3)^{\frac{2}{3} - (1-f)(1+\Delta^2)}]}{1 - f}, \quad (2.7)$$

The different boundary curves proposed above are shown in figure 2.1. The capillary number in this case was taken as the average value of Ca over the range of We in this study. The Oh value remains constant here, i.e., $Oh = 0.07$.

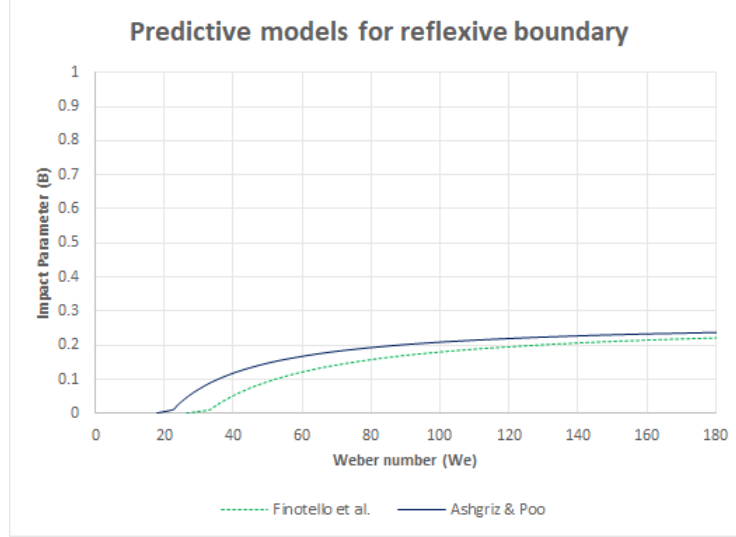


Figure 2.1: Boundary curves between coalescence and reflexive separation. $Ca = 0.06$

2.2 Theoretical description of stretching separation and models for the boundary curve between coalescence and stretching separation

Although there exist several models for predicting the boundary between coalescence and stretching separation in inviscid fluids, ([6], [23], [24]), the one presented by Ashgriz & Poo is considered here since it has been verified by numerous studies. Their model for stretching separation is based on the criterion that separation occurs if the kinetic energy is greater than the total surface energy. The boundary curve is given by,

$$We = \frac{4(1 + \Delta^3)^2[3(1 + \Delta)(1 + B)((\Delta^3\phi_s) + \phi_l)]^{\frac{1}{2}}}{\Delta^2[(1 + \Delta^3) - (1 - B^2)(\phi_s + \Delta^3\phi_l)]}, \quad (2.8)$$

where ϕ_s and ϕ_l are, geometrical factors depending on the parts of the droplets interacting during collision, given by,

$$\phi_s = \begin{cases} 1 - \frac{1}{4\Delta^3}(2\Delta - \tau)^2(\Delta + \tau) & \text{for } h > 1/2D_s \\ \frac{\tau^2}{4\Delta^3}(3\Delta - \tau) & \text{for } h < 1/2D_s \end{cases}, \quad (2.9)$$

where τ & h are given by,

$$h = \frac{1}{2}(D_l + D_s)(1 - B), \quad (2.10)$$

$$\tau = (1 - B)(1 + \Delta). \quad (2.11)$$

There are two other models, presented by Jiang *et al.* [8] and Finotello *et al.* [22] which take into consideration the effects of viscosity. The equation for the boundary proposed by Jiang *et al.* is given as,

$$B = \frac{C_5}{We^{1/2}}[1 + C_6 \frac{\mu}{\sigma}(\frac{\rho D}{\sigma})^{1/2}] \quad (2.12)$$

Here it was assumed that the two droplets act as two sliding bodies where, the surface tension force and the viscous force act against their momentum. Gotaas *et al.* [20] calculated values of constants, C_5 and c_6 in equation 2.12 by fitting the curve to their experimental data, finding them to be valid for both viscid and inviscid fluids.

Finotello theorized that for stretching separation, the initial kinetic surface energy of the two droplets is converted to the increased surface energy of the post collision droplets and satellite droplets and their new kinetic energy, but a significant amount of energy is also lost because of viscous dissipation. By running simulation models, they concluded that the fraction of energy lost to viscous dissipation depends largely on the impact parameter (B) and the capillary number (Ca) and is not influenced by We , especially for low Ca cases ($Ca < 1$). The fraction of energy lost to viscous dissipation, was found to have a linear relation to the impact parameter,

$$a_1(1 - a_2B),$$

where the coefficients (a_1 and a_2) depend on the capillary number. These coefficients were found empirically based on their simulations. It was further assumed that at

the boundary between coalescence and separation, the total surface energy before the collision and the surface energy just before separation occurs remain the same because the amount of new surface created is very minor. At the point of separation, the kinetic energy of the system was assumed to be negligible. The equation for their model is given as,

$$\frac{\frac{We\Delta^2}{12(1+\Delta^3)(1+\Delta^2)}}{\frac{We\Delta^2}{12(1+\Delta^3)(1+\Delta^2)} + 1} = a_1(1 - a_2B), \quad (2.13)$$

where,

$$a_1 = \frac{21}{22}(Ca^{\frac{1}{22}}), \quad (2.14)$$

and,

$$a_2 = \frac{1}{1 + \frac{1}{4}Ca}. \quad (2.15)$$

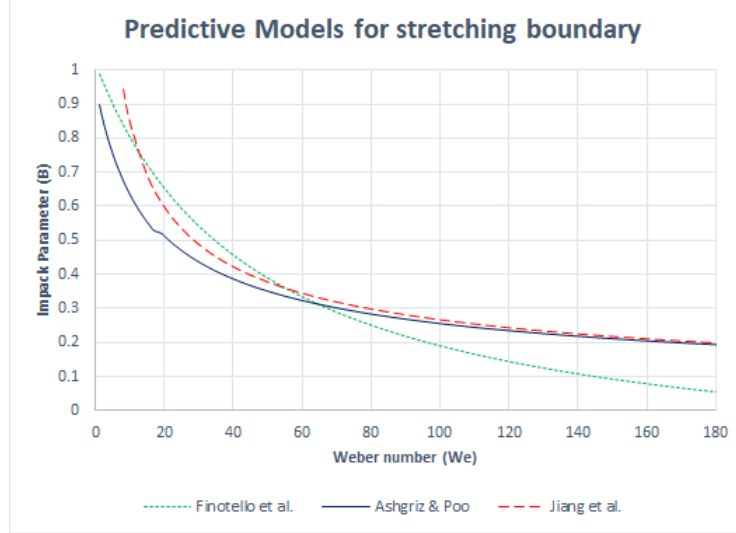


Figure 2.2: Boundary curves between coalescence and stretching separation. $Ca = Oh\sqrt{We}$

Chapter 3

Experimental Design

This chapter describes the experimental setup used to study the collision of burning droplets. Xylene droplets were generated using two piezoelectric droplet generators and ignited by a spark between two tungsten filaments. The collision event was recorded by a high-speed camera and the data was analyzed using a MATLAB script.

3.1 Droplet generation and Ignition

Figure 3.1 shows the schematic diagram of the experimental set-up as viewed from the direction of the high-speed camera. Two piezoelectric droplet generators provided a steady supply of isolated monodispersed xylene droplets. The working principle of the droplet generators has been detailed by Ulmke *et al.* [25], [26], and the LabVIEW program (figure 3.2) used to operate them has been developed by Riefler & Wriedt [27]. The two droplet generators were placed vertically pointing at each other and were both connected to the same signal generator. This ensured synchronized generation of both the droplets. The diameter of the droplets varied from $85\mu m$ - $95\mu m$.

This variance can be attributed to the variation in the Voltage impulse length among different experimental runs. It must also be noted that this is the diameter of the upper, non-burning droplet (D_l). The diameter of the lower droplet when ejected is $100\mu m$. After ignition, the droplet shrinks constantly. The droplet diameter at the point of collision (D_s) varies since the distance traveled by the burning droplet from ignition to collision is not constant. However, the diameter ratio (Δ) ranges from 0.8 - 0.9.

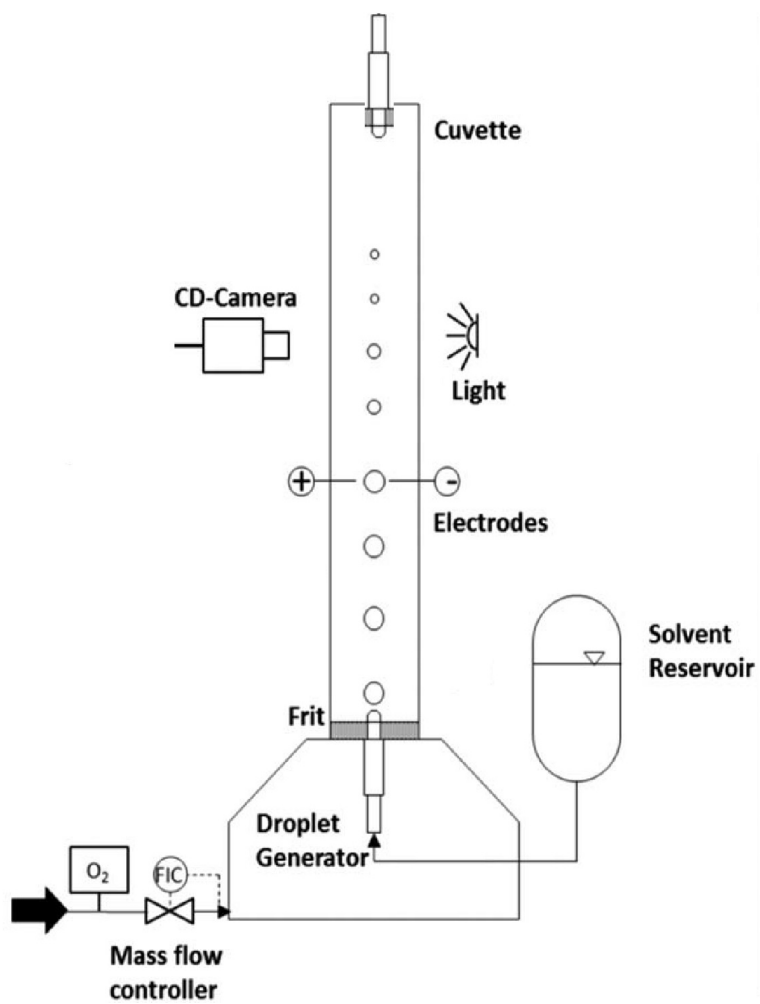


Figure 3.1: Experimental setup showing the layout of the droplet generators from the point of view of the high-speed camera [2]

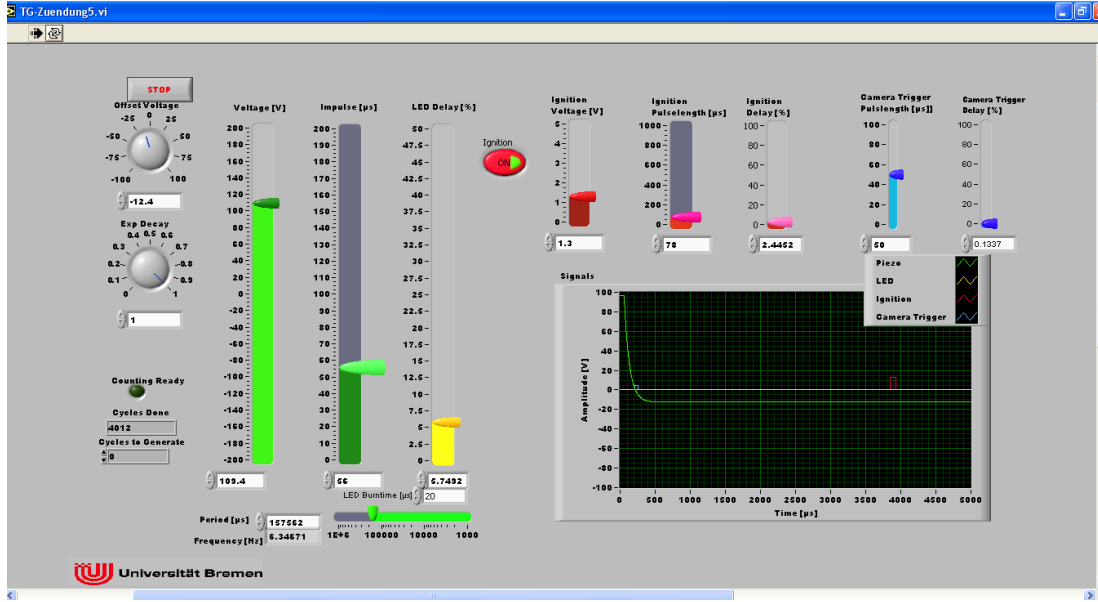


Figure 3.2: LabVIEW interface for controlling the signal sent to the droplet generators, LED strobe and ignition system.

Droplet velocities and therefore the collision Weber number can be varied by changing the current supplied to the piezoelectric droplet generator. Because of minor imperfections in the droplet capillaries and other unknown reasons (possibly erosion and depolarization of piezoelement [28]), the parameters required to generate stable droplet streams varies from time to time, leading to a slight variation in the droplet diameters. The droplets were generated at a frequency of 6 Hz . This means the separation between two successive droplets with diameters, $D_s = 90\text{ }\mu\text{m}$ (for the lower droplet) is given by $S = 1845\text{ }D_s$. This ensures that there is no interference between successive droplets, which can occur for $S \ll 100D_o$ in air [29] and well as in oxygen [30]. Thus, the droplet combustion and the entire collision event can be considered an isolated event. The fuel is supplied to the piezodropper from a small reservoir and the droplets are ejected into a quartz cuvette. The dimensions of the cuvette are $10 \times 10 \times 50\text{ mm}$ ($L \times W \times H$). The lower droplet passes through a 3 mm gap in between two tungsten filaments. The droplet is then ignited using a synchronized spark. This spark tends to alter the droplet trajectory and velocity. To minimize this, the spark duration and energy is lowered to a point where it is just enough to achieve ignition. Oxygen (99.5%) is supplied from

below the lower droplet generator through a porous frit to avoid fluctuations in the droplet trajectory and to achieve plug flow conditions. A mass flow controller is used to maintain the flow rate of $0.4L/min$.

This entire setup is mounted on a platform that can be raised or lowered. This is used to change the height of the setup, as required, to ensure the entire collision process is captured by the high-speed camera. This platform is in turn mounted on a micro-metric plate such that the distance of the collision event from the high-speed camera can be changed to make sure the images are in focus. On top of the platform, the lower droplet generator is placed on a micro-metric plate such that it can be moved laterally in the collision plane. The upper droplet generator is also mounted on a micro-metric plate, such that it can move transversely in an orthogonal plane. This is used to achieve collision of both the droplets since the point of collision changes as the droplet velocities are changed. The collision impact parameter (B) is also varied by using this mechanism. The upper droplet generators height, with respect to the lower droplet generator, can be varied independently. This entire system is used to achieve collision of the two droplets before the lower droplet extinguishes.

3.2 Image acquisition system

Two cameras are used in this study. A Charge-Couple-Device (CCD) camera in conjunction with a strobe is used to help adjust parameters to ensure that the droplet trajectories are in the same plane so that collision takes place. A high-speed camera is used to record each collision event and this data is used to calculate droplet sizes and velocities.

As seen in figure 3.1, the CCD camera is placed perpendicular to the high-speed camera and it views the droplets along the collision plane. An LED strobe acts as the back-light for the CCD camera. Both, the LED and the camera shutter are synchronized with the droplet generators. The LED delay can be increased to view the droplets at successive positions.

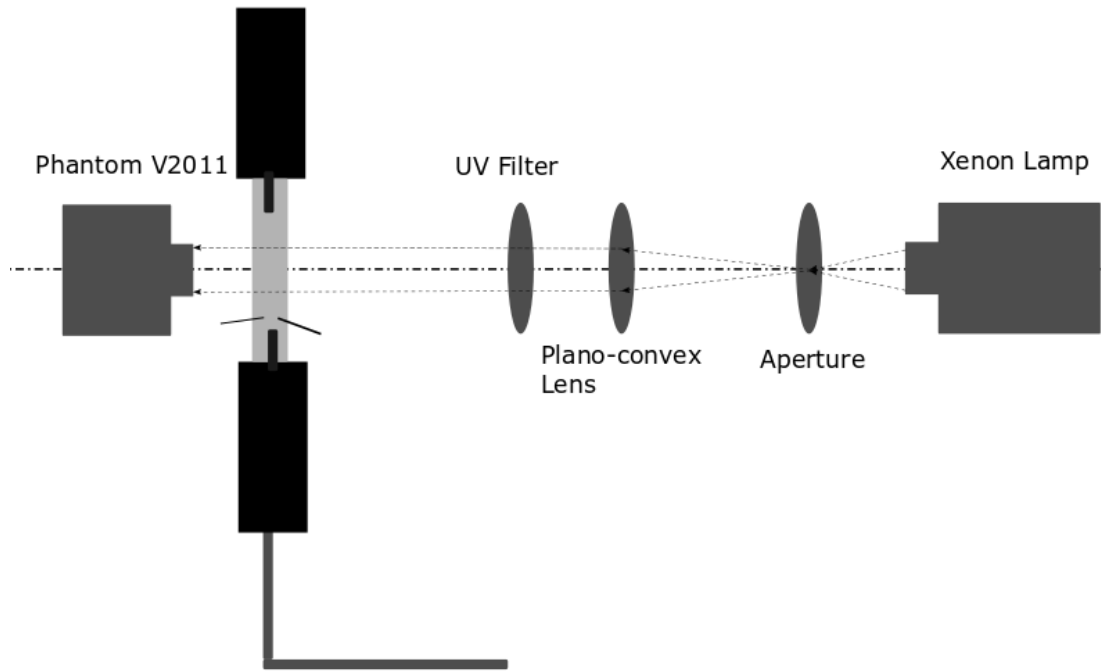


Figure 3.3: Layout of the optical system to record high-speed images

Figure 3.3 shows the schematics of the high-speed camera and the light source. The camera used is the Phantom V2011 by Vision Research, which can record at frame rates up to 70,000 fps at a resolution of 512x512. The CMOS sensor has a pixel size of $28\ \mu\text{m}$. This camera is attached to a microscopic lens with zoom levels up to 10x. This provides a close-up view, at very high frame rates, of the collision event. Because of the high zoom and the extremely high frame rates, the exposure time is very low. To get enough lighting a bright light source is required. An Oriel instruments illuminator with a 300 W Xenon lamp acts as a permanent light source. The observation technique used is shadowgraphy. The light passes through an aperture and then onto a plano-convex lens ($f = 100\ \text{mm}$). A UV filter lens is placed after the plano-convex lens to block the UV radiation from the light source. This system provides highly collimated light rays to the camera.

3.3 Image Processing

A MATLAB script analyzes the recorded videos of the collision process. The videos are saved in a manner such that they include at least one frame with no droplet present in the field of view of the camera. This image was then subtracted from every consecutive frame to get rid of any dust or smudges present on the microscopic lens or the cuvette. This also converted the remaining frames to grayscale with a high contrast. After this the images were further processed to remove any remaining background grains. Once an image had gone through pre-processing, MATLABs inbuilt function, *imfindcircles* was used to detect the droplets in the frames. This function detects the droplets edges and by calculating the diameter of the circle along various orientations, locates the center. This data was used to measure the droplet diameters and the co-ordinates of the droplet centers in each consecutive frame.

Using this method, the error range for droplet diameter calculations is 1 pixel which equates to $2.8 \mu m$. Droplet velocities and trajectories are then calculated by using the co-ordinates of the droplet centers collected by the MATLAB script. This data is also used to calculate the Impact parameter (B). The calculated values agree well, when compared with values obtained by using the built-in object detection and motion estimation software provided by Vision Research. The high-speed camera saves the videos in the *.cine* format. This file contains additional information regarding the recorded video, such as the frame rate. Once the phantom libraries are loaded on MATLAB, this information could be used to directly calculate the droplet velocities even if the videos were recorded at different frame rates. The entire MATLAB code is included in the Appendix for more details.

3.4 Experimental procedure

Because of the extremely small size of the droplets, the fluctuations in the supply current parameters to produce a stable droplet and, the trajectory deflection caused by spark ignition, achieving successful collision post ignition requires many experiments. The following experimental procedure needs to be followed with diligence:

1. The working fluid is pushed through the nozzles of both the droplet generators using a syringe, until a steady stream of the liquid flows out, to make sure there are no air bubbles trapped inside the nozzles.
2. The height of the CCD camera and the LED delay should be adjusted so that both the droplets are in the CCDs field of view.
3. The cuvette walls are then cleaned with acetone to make sure recorded images are bright and clear.
4. Next the two droplets are brought next to each other, and the upper droplet generator is moved till it is on the collision plane.
5. The high-speed camera is now switched on, and the entire set-up is moved (if needed) to bring both the droplets in focus.
6. The ignition system is then started, but O_2 is kept off. The droplet does not always ignite; and in such a case, the electrodes must be moved to make sure the droplet is passing in between them. The ignition delay may also need to be changed to make the spark occur while the droplet is in between the electrodes.
7. The O_2 is kept off so that the droplet can be seen on the CCD screen; and the ignition delay, voltage amplitude, or the voltage supplied are varied slightly to achieve minimum droplet fluctuation. Once the O_2 is turned on, only a streak of the burning droplet is visible on the CCD screen. Although the droplet ignites in the absence of O_2 , the flame extinguishes almost immediately and the droplet is visible on the CCD screen.
8. Once the droplet is stable and collision has been achieved, the O_2 supply is turned on. Video can now be recorded on the high-speed camera.
9. The high-speed camera records a video for just over a second. This means that each recording has 6 collision events occurring in it. The video is then played, and each collision event is isolated and saved in different cine files. At this stage, some collision events might be discarded because of reasons to be explained later.

10. Once the required number of videos are saved, the lower droplet is moved slightly so that more videos can be recorded at different values of B .
11. To record data at a different Weber number, ignition is turned off; and the supply voltage is changed. Steps 1-10 are then repeated.

To ensure that the collision process is two-dimensional, both the droplets are aligned such that their velocity vectors fall on a plane perpendicular to the high-speed camera. This is called the collision plane. Because of deflections caused by the spark, sometimes the trajectory of the lower droplet is offset from the plane. This can be detected by examining the video for any asymmetry in the droplet evolution and checking for any motion of the evolved droplets in a direction perpendicular to the collision plane. This is done before saving the individual collision files at step 9.

3.5 Working fluid and thermo-physical properties

The working fluid used in the present study is xylene. Although the fluid is made up of a mixture of the three isomers of xylene; m-xylene, o-xylene and p-xylene, the major composition of the mixture is m-xylene. Thus, the properties of m-Xylene are used wherever necessary.

Since the lower droplet is burning, the surface temperature is assumed to be at boiling point ($T_b = 412K$) [31]. Thus, the properties at this temperature are computed and used to calculate the various non-dimensional numbers. Since the boiling point of all the isomers are around the same, the actual surface temperature should not deviate much from this assumed value. Table 3.1 provides the properties of m-xylene at $T_b = 412K$.

Fluid	Surface Tension (N/m)	Density (kg/m^3)	Viscosity ($mPa - s$)
m-xylene	0.016	765.84	0.2255

Table 3.1: Properties of m-xylene at $T = 412K$

It is worth noting that the temperatures of the two droplets are not the same. The

upper droplet does not ignite at the point of collision and thus the surface temperature is less than the boiling point. However, since the strength of the interacting region between the two droplets determines coalescence or separation, this can only be as strong as the surface tension of the weaker droplet [\[12\]](#).

Chapter 4

Results and discussions

In this chapter, results from the droplet collision experiments are discussed. First, we compare images from the experiments with the post-processed images for droplet detection to validate the MATLAB script. Next, a qualitative analysis is shown of the effects of Weber number number and impact parameter on the various collision regimes and the flame structure. Finally, data from the current experiments is compared with the models discussed in chapter 2.

4.1 Image processing and droplet tracking

To capture every aspect of the collision process, the high-speed camera recorded the collisions at a frame rate of just over 67,000 fps. The time between two frames is $14.92 \mu s$. This means that the frame exposure time should be very low. The exposure time for each frame is just under $6 \mu s$. Very strong lighting is necessary to make sure that the contrast between the droplets and the surroundings is high enough for post-processing of the images to work effectively. The images are recorded at a resolution of 515x512, in gray scale at 12 bits per pixel. Figures 4.1a & 4.1b show a frame containing both the droplets before and after processing, respectively. The lower and upper droplets, as detected by the MATLAB script, are represented by the blue and green circles respectively. As figure 4.1 shows, the droplets are detected very accurately and this is confirmed by comparing the MATLAB data on a few videos with manual calculations made by using the object detection and tracking software in the Phantom cine viewer. The maximum error in making droplet diameter measurements is 2 pixels ($5.6 \mu m$). The function *imfindcircles* is used with the the edge threshold set at 0.25; and the method set to 'Two Phase'.

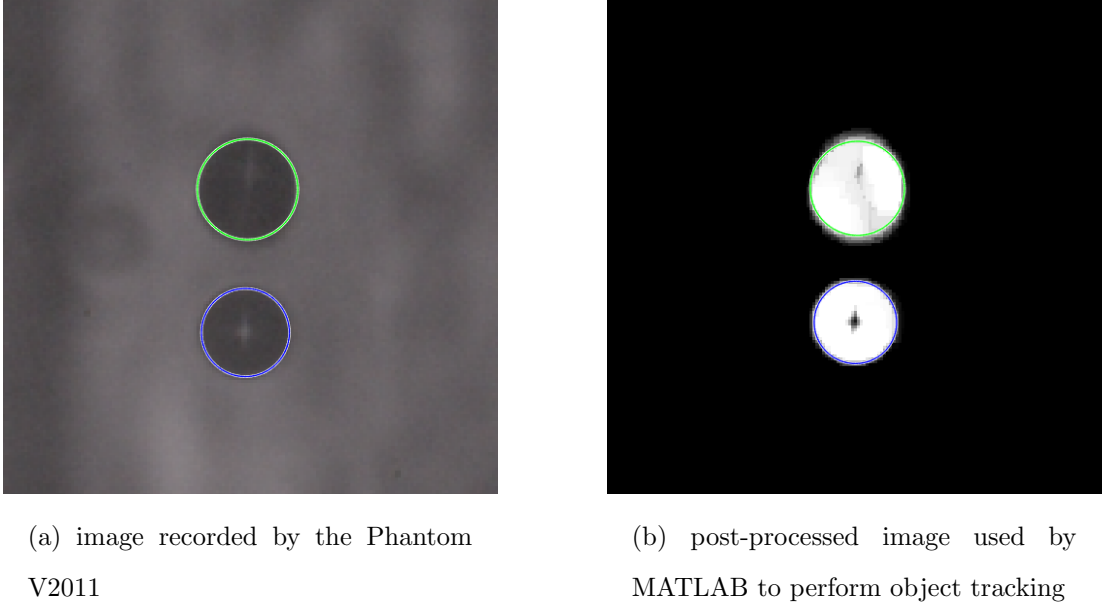


Figure 4.1: Comparison of the raw image with the post-processed image. The blue and green circles are the circles detected by MATLAB.

The droplet velocities are calculated by using the center co-ordinates to measure the x and y components of the individual droplet velocities. A least squares fit is used to measure the droplet trajectories and velocities.

4.2 Droplet and flame evolution for various collision regimes

The collision outcomes in the present study fall in three distinct regimes. These regimes resemble the regime map for water droplets shown in figure 1.2a. Since collisions at very low Weber numbers ($We < 20$) could not be performed in the current setup, there is not enough data to confirm the existence of regimes I & II. Figure 4.4 shows the collision sequences of various outcomes at different Weber numbers.

Because of the low exposure times, very bright backlighting is used to record the images. This made it very difficult to see the flame around the the burning droplet. Rosebrock *et al.* [2] conducted experiments on burning droplets of xylene and studied the flame. Figure 4.2 shows that the xylene droplet burns with a round sooty flame. It is also discussed that the level of soot diminishes as the droplet diameter decreases. It is important to maintain appropriate O_2 flow rate. A very high flow rate results in the

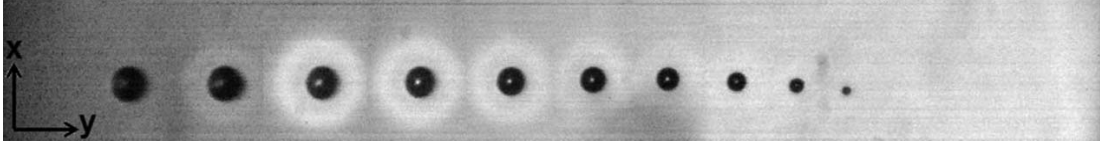


Figure 4.2: Flame structure of a xylene droplet burning in Oxygen coflowing at 0.4 L/min. Image recorded by Rosebrock *et al.* [2]

droplet burning out before collision can occur.

For a fixed impact parameter, collision outcomes depend on the Weber number. Its effects on the flow of the intermediate gas layer trapped between two colliding droplets will be discussed in detail in the following subsections. The flow field of this gas layer and the liquid from both droplets are important in the present study since the gas trapped here is xylene vapor. The flow of this trapped gas and the flow of the liquid from each droplet guide the progression of the flame after collision. Apart from the Weber number, these flow fields also depend on the density of the gas trapped, the droplet diameter ratio, and the viscosity of the liquid. Since the Weber number is our control parameter and the rest of the properties are fixed in the current experiments, we will only look at the Weber effects at different impact parameters.

Nikolopoulou *et al.* [4] [32] [3] have conducted extensive numerical studies on this topic. Their simulations provide significant details regarding the flow of fluids during collision, which are otherwise not visible experimentally. Results from their numerical studies will be used as a guide to explain the behavior of the colliding droplets in the current experiments and also the spread of the flame immediately after collision.

Because of the flame surrounding the lower droplet before collision, it can be assumed that the gas present in the region in between the two colliding droplets is xylene. It has further been noted by Rosebrock *et al.* [2] that soot formation in the xylene flame, reduces reaction rates and leads to a build up of fuel vapor between the flame and the droplet. The flow of this vapor after collision guides the post-collision flame.

4.2.1 Head-on or nearly head-on collisions

According to the model proposed by Ashgriz & Poo [7], the critical Weber number, for this study, beyond which head-on collisions result in reflexive separation is 18.7. Since we do not have experimental data for Weber numbers lower than this, all head-on collisions in this study resulted in reflexive separation. Although for some low Weber number collisions, with impact parameters less than 0.3, the droplets coalesce permanently. Examples of these collision outcomes are given in figures 4.4a to 4.4f

For head-on collisions, the droplets flatten at the point of contact and form a circular disc. As seen in figure 4.4a, the disc reflexes back because of the surface tension forces and forms an elongated cylinder. At this point the momentum of the fluid makes it flow towards the two ends of the cylinder. Once the cylinder reaches its maximum length (determined by the initial kinetic energy), the surface tension forces again start countering the outward momentum and the fluid changes direction. This leads to the separation of the first two droplets. For higher Weber numbers, the cylinder is stretched to a greater extent and this causes capillary waves to form in the connecting bridge, as seen in figure 4.4c. These capillary waves result in the formation of additional satellite droplets.

Simulations done by Nikolopoulos *et al.* [3] show that at the point of collision, the gas trapped in between the two liquid surfaces tries to escape, forming a sheet of gas jet between them. This gas jet forms vortex rings outside the droplet bodies as shown in figure 4.3. A high pressure region develops around the gas bubble trapped in between the two droplets. The presence of micro bubbles within the coalesced mass is shown by Ashgriz & Poo [7] experimentally and by Premnath & Abraham [33] numerically. The gas bubble is then squeezed out by the fluid flowing outward inside the droplet. The velocity of the gas jet is found to be on the order of 10 times the relative velocity of the colliding droplets and increases with a decrease in fluid viscosity. The sudden appearance of a highly sooty flame immediately after the coalesced droplet reflexes and separation occurs in figures 4.4a, 4.4b and 4.4c suggests that the xylene vapor accumulates around the initial coalesced mass and ignites in that region forming

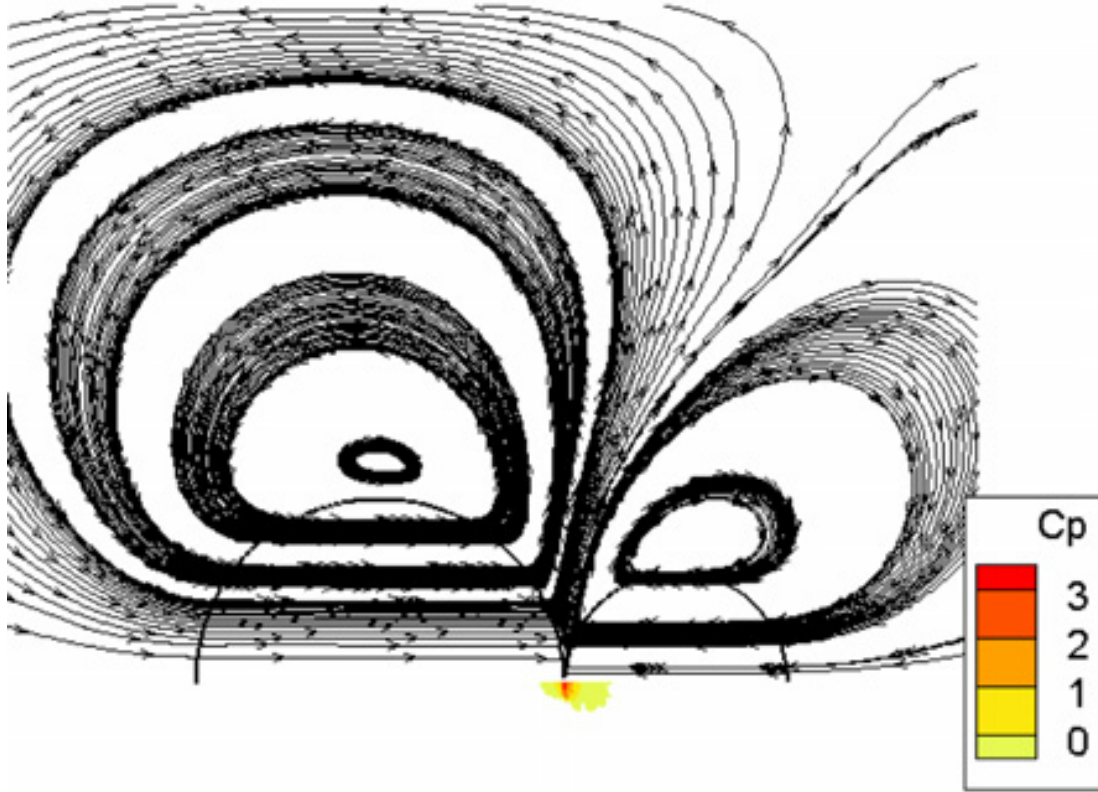
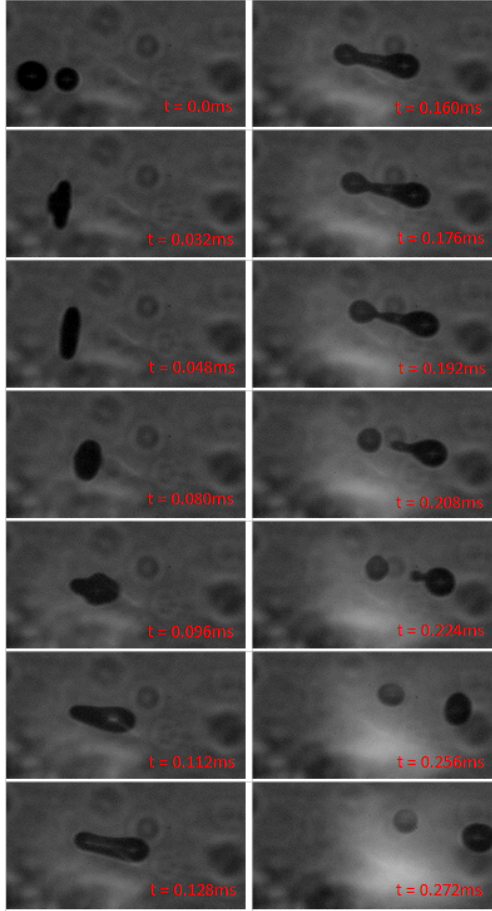


Figure 4.3: Formation of vortex rings and pressure distribution. Image by Nikolopoulos *et al.* [3]

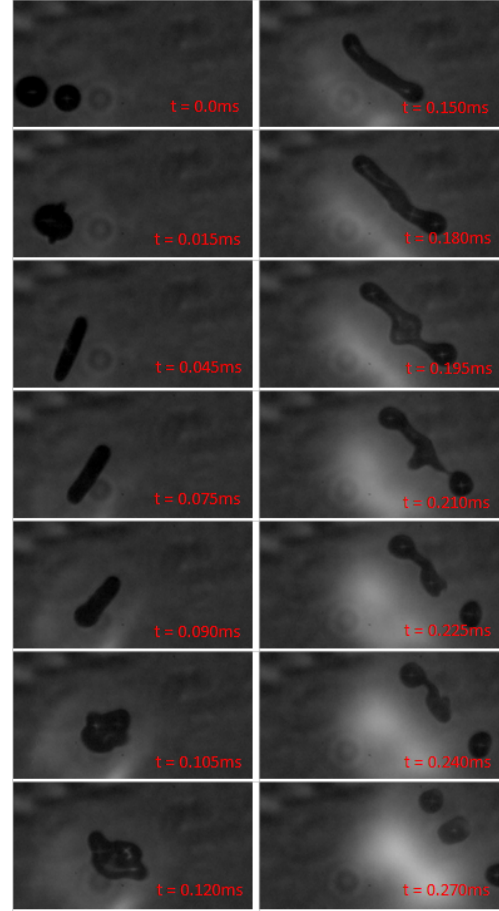
a flame with high soot content at the location of the collision event even after the droplets have moved away from that point. Similar phenomenon is seen in figure 4.4f where coalescence occurs at a low impact parameter.

4.2.2 Off-center collisions

Off-center collisions result in either coalescence, for low impact parameters, or stretching separation, for higher impact parameters. Figure 4.4d shows a collision sequence at $We = 47.12$ and $B = 0.23$. Here, the off-center collision of the two droplets leads to the formation of a disc similar to the one formed for reflexive separation. In this case though, since the collisions are off-center, the disc assumes a donut shape with a thin layer of liquid in the center. This sheet of liquid initially stretches outward and then gets pulled back towards the center resulting in it getting raised out of the plane of the

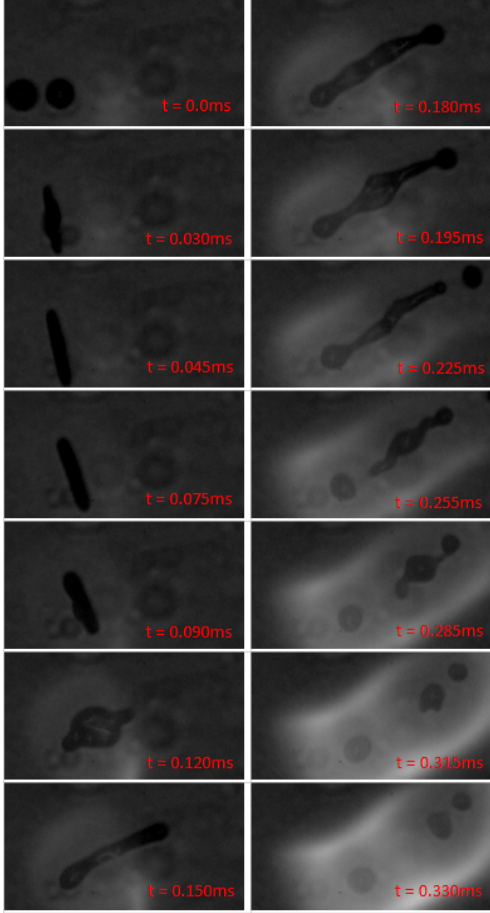


(a) reflexive separation, $We = 49.25$, $B = 0.003$, $\Delta = 0.75$, $V = 3.95$ m/s

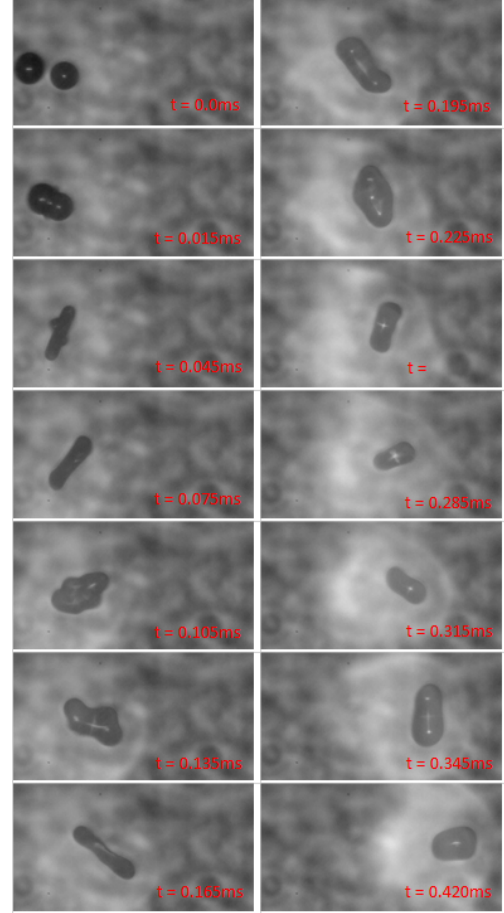


(b) reflexive separation, $We = 93.65$, $B = 0.16$, $\Delta = 0.82$, $V = 5.04$ m/s

Figure 4.4: Collision images from the high-speed camera. The smaller burning droplet is moving from right to left while the larger droplet is moving from left to right

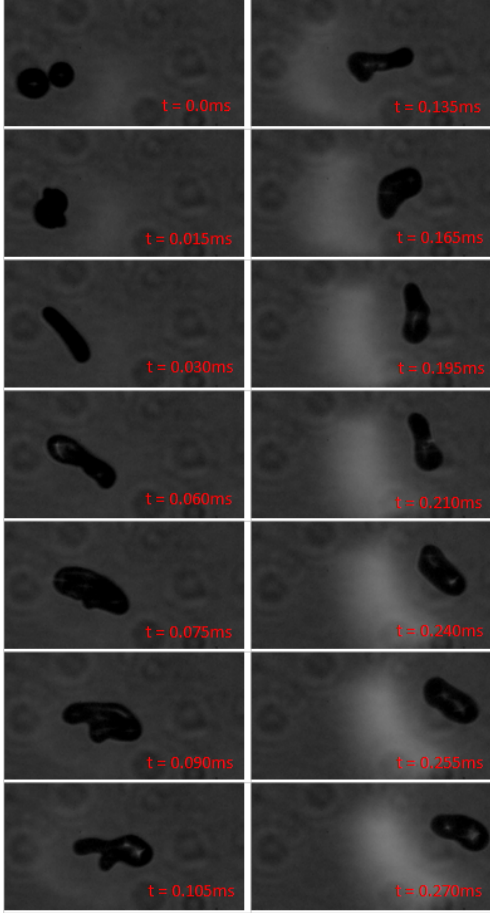


(c) reflexive separation, $We = 135.24$,
 $B = 0.01$, $\Delta = 0.94$, $V = 5.67$ m/s

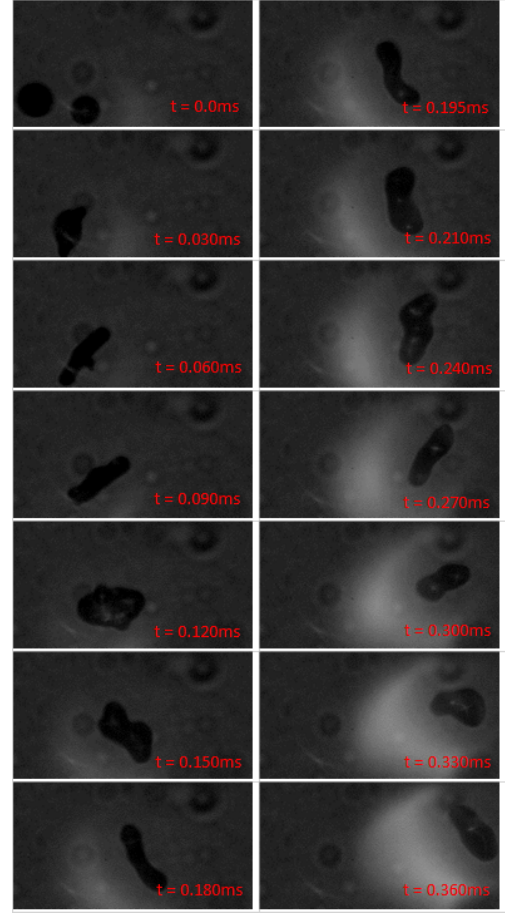


(d) coalescence, $We = 47.12$, $B = 0.23$,
 $\Delta = 0.875$, $V = 3.57$ m/s

Figure 4.4: Collision images from the high-speed camera. The smaller burning droplet is moving from right to left while the larger droplet is moving from left to right



(e) coalescence, $We = 74.6$, $B = 0.35$,
 $\Delta = 0.875$, $V = 4.5$ m/s



(f) coalescence, $We = 117$, $B = 0.18$,
 $\Delta = 0.83$, $V = 5.44$ m/s

Figure 4.4: Collision images from the high-speed camera. The smaller burning droplet is moving from right to left while the larger droplet is moving from left to right

donut. This can be seen in figure 4.4d at $t = 0.045$ ms. This sheet of liquid reflexes within the center of the donut until it finally connects with the outer ring at $t=0.075$ ms and eventually leads to stable coalescence. The ability of this disc to achieve coalescence decreases with an increase in the droplet velocities and thus the collision Weber number. From this point on until $t=0.420$ ms, the coalesced mass oscillates in the collision plane or in a plane perpendicular to the collision plane as can be seen by the deformations in the images leading up to the formation of a stable spherical droplet.

Similar to the previous case, at the time of contact of the two droplets, the gas between them is squeezed out in the form of a jet sheet. This leads to entrainment of the surrounding gas and vortices are formed around the surface of each droplet. Nikolopoulos *et al.* [4] performed numerical simulations on collision of n-heptane droplets with a diameter of $356\mu\text{m}$. Figure 4.5 shows the flow fields of the gas jet around the droplet for a collision at $We = 70.8$ and $B = 0.25$, where the collision plane is the x-z plane. For low weber numbers, the droplets coalesce quickly and the entrained xylene vapor forms a swirling flame around the rotating droplet. Such a flame is visible in the collision images shown in figure 4.4d.

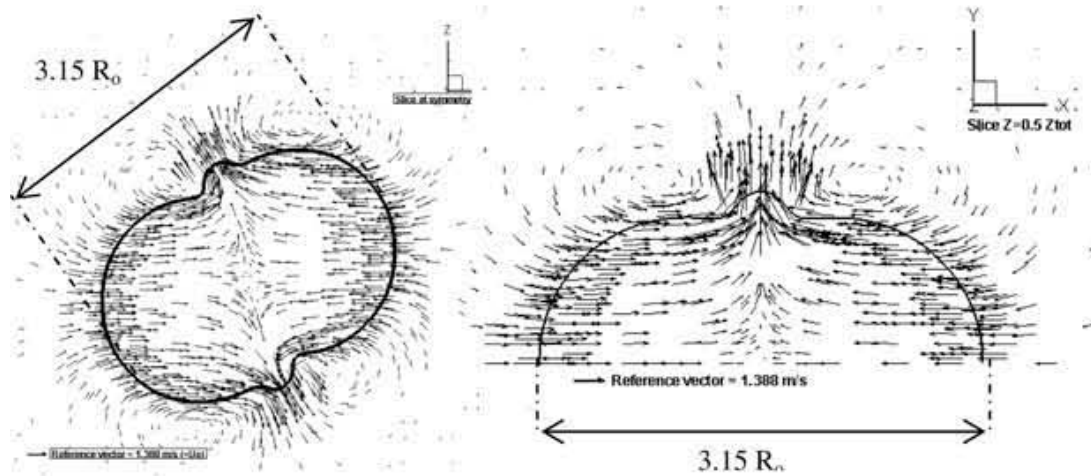
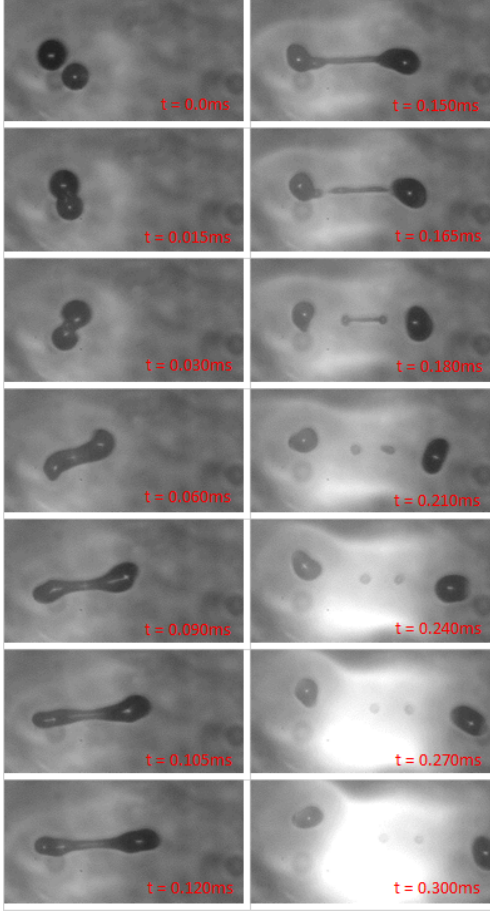
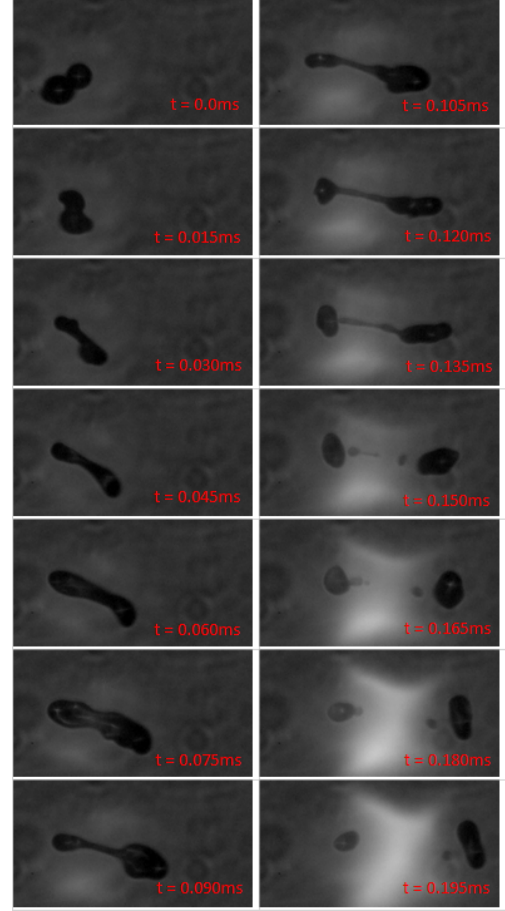


Figure 4.5: Formation of vortices around the gas jet squeezed out during collision. R_0 is the initial droplet radius. Image by Nikolopoulos *et al.* [4]

Figure 4.5b shows stretching separation at a relatively low impact parameter, B

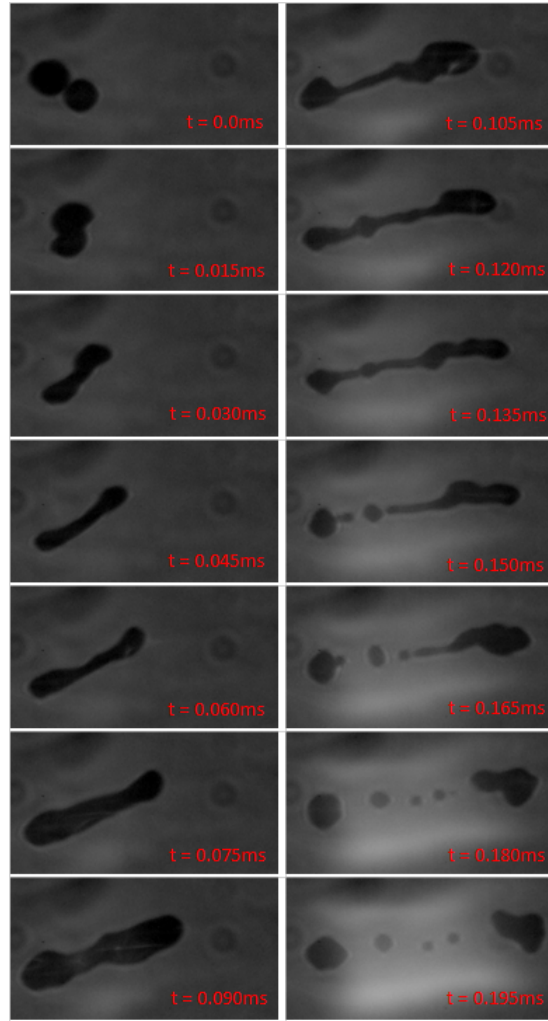


(a) stretching separation, $We = 45.67$,
 $B = 0.74$, $\Delta = 0.875$, $V = 3.52$ m/s



(b) stretching separation, $We = 90.67$,
 $B = 0.44$, $\Delta = 0.93$, $V = 4.8$ m/s

Figure 4.5: Collision images from the high-speed camera. The smaller burning droplet is moving from right to left while the larger droplet is moving from left to right



(c) stretching separation, $We = 140.5$,
 $B = 0.5$, $\Delta = 0.88$, $V = 5.96 \text{ m/s}$

Figure 4.5: Collision images from the high-speed camera. The smaller burning droplet is moving from right to left while the larger droplet is moving from left to right

$= 0.44$ and a slightly high weber number, $We = 90.67$. Figure 4.5a shows stretching separation at high impact parameter ($B = 0.74$) but a low weber number ($We = 45.67$). Here, the initial deformation is similar to the case of off-center coalescence collisions. The droplets rotate around an axis perpendicular to the collision plane. The initial momentum of the rotating mass pulls the liquid towards either ends of the central mass, thus stretching the connecting liquid. The connecting bridge keeps lengthening until the surface tension energy is able to oppose the droplet momentum and pull the liquid back towards the center of the bridge. This leads to pinching at the thin ends of the bridge as seen at $t = 0.165$ ms in the first figure. Thus, two resulting boundary droplets are formed. The connecting ligament experiences two opposing forces, i.e., the surface tension pulling the ends towards the center, to form a central droplet, while the liquid at the center keeps flowing towards the ends because of its momentum, pulling the central bridge towards the edges. This leads to the formation of two satellite droplets from the fluid in the connecting bridge.

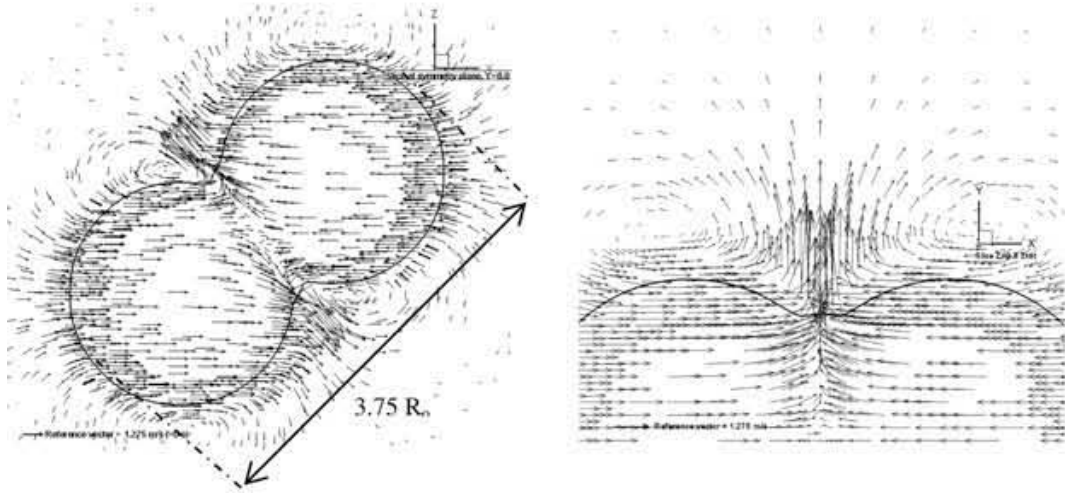


Figure 4.6: Formation of vortices around the gas jet squeezed out during stretching separation at low impact parameters. R_0 is the initial droplet radius. Image by Nikolopoulos *et al.* [4]

Figure 4.6 shows the flow field of the gas around the colliding droplets at the point of collision. Nikolopoulos *et al.* [4] reported that similar to the earlier cases, when the

two droplets first collide, the gas between them is squeezed out to form a jet sheet because of flattening of the two liquid surfaces. Vortices are formed around both the sides of the jet sheet, close to the surfaces of the droplets, because of entrainment of the surrounding gases. Vortices in the opposite direction are seen around the liquid bridge (figure 4.7). This explains the formation of a bright sooty flame around the ligament in Figure 4.5b at $t = 0.090$ ms. Xylene vapor gets accumulated around the central filament because of the opposing vortices hugging close to the surface; and a small portion gets transported around the two boundary droplets forming a dim flame around them. The disintegration of the filament suddenly increase the flame intensity because of the formation of smaller satellite droplets that are quickly burned off.

Figure 4.5c shows a very high Weber number collision. The mechanics of separation and flame formation in this case are the same as the earlier cases. In this case, however, because of the high relative velocity, the central filament is stretched for a far greater length than in the previous two cases. This results in multiple satellite droplets forming based on the same principles as the previous case. The vapor distribution around these droplets follows the same mechanics too as can be seen by the formation of a similar flame around the connecting filament and the two edge droplets.

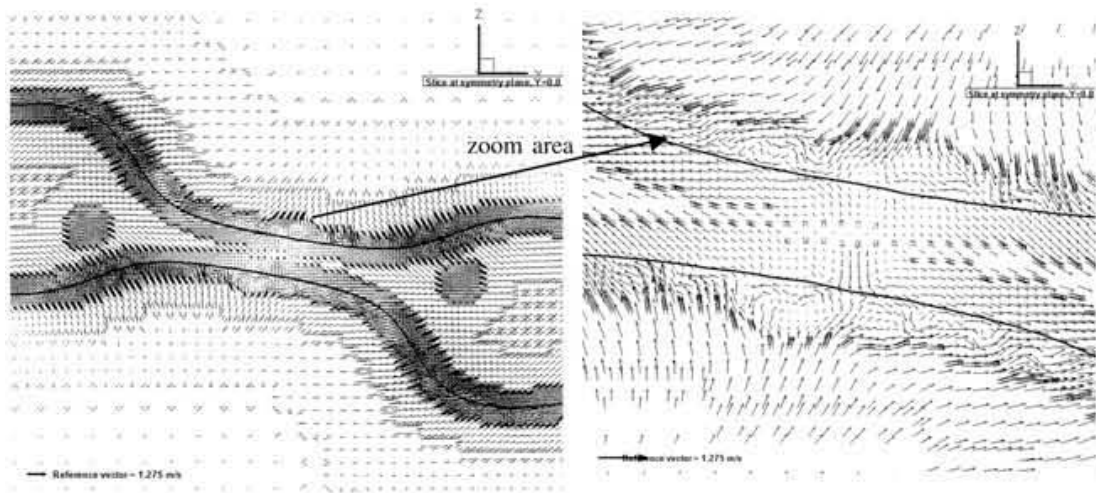


Figure 4.7: Formation of vortices around the connecting ligament during stretching separation at low impact parameters. R_o is the initial droplet radius. Image by Nikolopoulos *et al.* [4]

4.3 Comparison of experimental data with analytical models

As discussed in Chapter 2, various phenomenological models are available in literature. Since none of the models were proposed for collision of burning droplets, experimental data from the present study is compared with the proposed models to evaluate whether the presence of the flame causes any changes in the observed collision regimes.

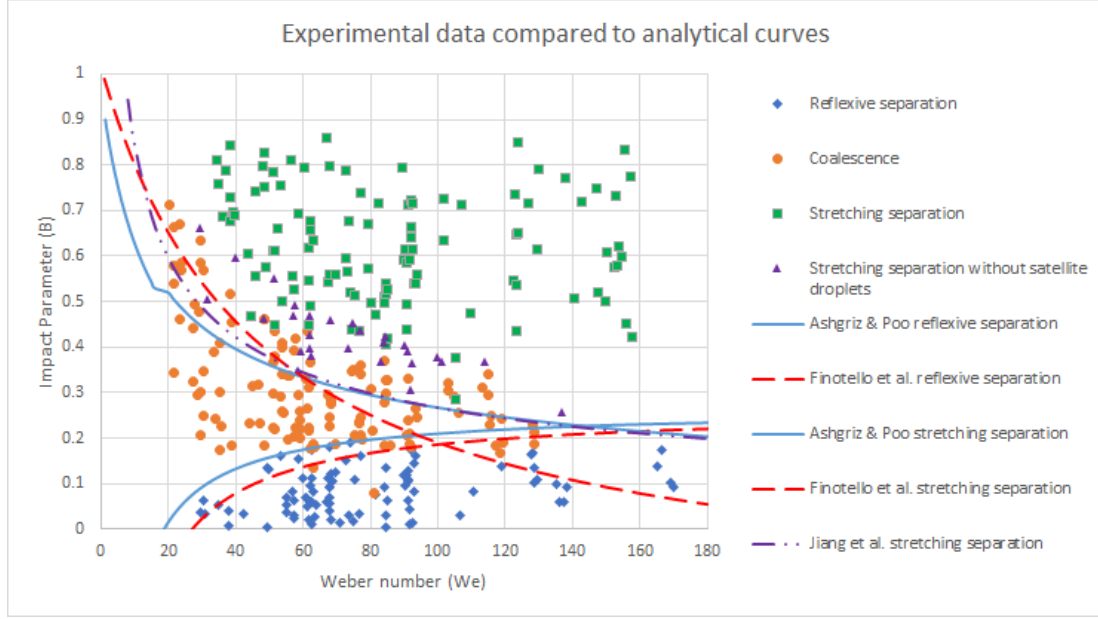


Figure 4.8: Experimental data compared to phenomenological boundary curves

Figure 4.8 shows the experimental data on a We-B plot along with the various analytical curves. The curve for the coalescence-reflexive separation boundary proposed by Ashgriz & Poo is a close fit to the experimental data. The slight over prediction of reflexive separation by this model is to be expected since the model assumes that there is no viscous dissipation at all. On the other hand, Finotello *et al.*'s model makes better predictions at higher weber numbers but under predicts in the initial lower weber range. More importantly, the critical weber number for the onset of reflexive separation is much higher than the one experimentally observed. This trend suggests that the effects of viscous dissipation are insignificant at lower Weber numbers but increasingly gain importance at Weber numbers over 100.

All three curves for the boundary between stretching separation and coalescence

heavily over predict the onset of separation. Amongst the three curves, the curve proposed by Ashgriz & Poo is highly inaccurate, particularly at low Weber numbers. This error can be attributed to the fact that viscous effects are not considered in their model. The other two curves are marginally better at predicting the onset of stretching separation, specially at low and intermediate Weber number around 60. This shows that viscosity does play an important role in determining the collision outcomes for this regime. The reason the two curves over predict separation could be attributed to the fact that the actual viscosity of the fluid might be slightly higher than assumed in this study, since the larger droplet is at a lower temperature and thus its viscosity must be higher. Also, temperature at the center of the burning droplet can be lower than that at the surface. This can also lead to higher surface tension in the connecting liquid bridge which is the point of separation for this regime.

Chapter 5

Conclusion and future scope

The present study provides new experimental data to study the flow pattern of the gas around colliding droplets. The behavior of the flame after collision could be adequately explained by results of numerical simulations of the flow field of gas around colliding droplets. Further experiments of collision of burning droplets can be used as an effective way to verify the numerical results which are otherwise difficult to observe experimentally. It was also shown that existing theoretical models are not sufficient to describe the boundary curves of collisions of burning droplets. Further experiments need to be conducted with different fuels and data for both burning and non burning cases under identical conditions should be compared. This can provide further insight into the parameters affected by the presence of a flame during droplet collision.

References

- [1] J Qian and CK Law. Regimes of coalescence and separation in droplet collision. *Journal of Fluid Mechanics*, 331:59–80, 1997.
- [2] Christopher D Rosebrock, Norbert Riefler, Thomas Wriedt, Lutz Mädler, and Stephen D Tse. Disruptive burning of precursor/solvent droplets in flame-spray synthesis of nanoparticles. *AIChE Journal*, 59(12):4553–4566, 2013.
- [3] N Nikolopoulos, G Strotos, KS Nikas, and G Bergeles. The effect of weber number on the central binary collision outcome between unequal-sized droplets. *International Journal of Heat and Mass Transfer*, 55(7):2137–2150, 2012.
- [4] N Nikolopoulos, A Theodorakakos, and G Bergeles. Off-centre binary collision of droplets: A numerical investigation. *International Journal of Heat and Mass Transfer*, 52(19):4160–4174, 2009.
- [5] JR Adam, NR Lindblad, and CD Hendricks. The collision, coalescence, and disruption of water droplets. *Journal of Applied Physics*, 39(11):5173–5180, 1968.
- [6] PR Brazier-Smith, SG Jennings, and J Latham. The interaction of falling water drops: coalescence. In *Proceedings of the Royal Society of London A: Mathematical, Physical and Engineering Sciences*, volume 326, pages 393–408. The Royal Society, 1972.
- [7] N Ashgriz and JY Poo. Coalescence and separation in binary collisions of liquid drops. *Journal of Fluid Mechanics*, 221:183–204, 1990.
- [8] YJ Jiang, A Umemura, and CK Law. An experimental investigation on the collision behaviour of hydrocarbon droplets. *Journal of Fluid Mechanics*, 234:171–190, 1992.
- [9] J-P Estrade, Hervé Carentz, G Lavergne, and Y Biscos. Experimental investigation of dynamic binary collision of ethanol droplets—a model for droplet coalescence and bouncing. *International Journal of Heat and Fluid Flow*, 20(5):486–491, 1999.
- [10] Melissa Orme. Experiments on droplet collisions, bounce, coalescence and disruption. *Progress in Energy and Combustion Science*, 23(1):65–79, 1997.
- [11] Rong-Horng Chen and Chiu-Ting Chen. Collision between immiscible drops with large surface tension difference: diesel oil and water. *Experiments in fluids*, 41(3):453–461, 2006.
- [12] T-C Gao, R-H Chen, J-Y Pu, and T-H Lin. Collision between an ethanol drop and a water drop. *Experiments in Fluids*, 38(6):731–738, 2005.

- [13] Keeney Willis and Melissa Orme. Binary droplet collisions in a vacuum environment: an experimental investigation of the role of viscosity. *Experiments in fluids*, 34(1):28–41, 2003.
- [14] N Ashgriz and P Givi. Binary collision dynamics of fuel droplets. *International journal of heat and fluid flow*, 8(3):205–210, 1987.
- [15] N Ashgriz and P Givi. Coalescence efficiencies of fuel droplets in binary collisions. *International Communications in Heat and Mass Transfer*, 16(1):11–20, 1989.
- [16] GDM MacKay and SG Mason. Some effects of interfacial diffusion on the gravity coalescence of liquid drops. *Journal of Colloid Science*, 18(7):674–683, 1963.
- [17] RM Schotland. Experimental results relating to the coalescence of water drops with water surfaces. *Discussions of the Faraday Society*, 30:72–77, 1960.
- [18] GDM MacKay and SG Mason. Some effects of interfacial diffusion on the gravity coalescence of liquid drops. *Journal of Colloid Science*, 18(7):674–683, 1963.
- [19] G Brenn, D Valkovska, and KD Danov. The formation of satellite droplets by unstable binary drop collisions. *Physics of Fluids*, 13(9):2463–2477, 2001.
- [20] Cecilie Gotaas, Pavel Havelka, Hugo A Jakobsen, Hallvard F Svendsen, Matthias Hase, Norbert Roth, and Bernhard Weigand. Effect of viscosity on droplet-droplet collision outcome: Experimental study and numerical comparison. *Physics of fluids*, 19(10):102106, 2007.
- [21] KG Krishnan and E Loth. Effects of gas and droplet characteristics on drop-drop collision outcome regimes. *International Journal of Multiphase Flow*, 77:171–186, 2015.
- [22] Giulia Finotello, Johan T Padding, Niels G Deen, Alfred Jongsma, Fredrik Innings, and JAM Kuipers. Effect of viscosity on droplet-droplet collisional interaction. *Physics of Fluids*, 29(6):067102, 2017.
- [23] R W Park. Behaviour of water drops colliding in humid nitrogen. *Ph.D. thesis*, 1970.
- [24] VA Arkhipov, GS Ratanov, and VF Trofimov. Experimental investigation of the interaction of colliding droplets. *Journal of Applied Mechanics and Technical Physics*, 19(2):201–204, 1978.
- [25] H Ulmke, T Wriedt, H Lohner, and K Bauckhage. The piezoelectric droplet generator—a versatile tool for dispensing applications and calibration of particle sizing instruments. In *Proceedings of the 1st International euspen Conference*, volume 2, pages 290–293, 1999.
- [26] Hartmut Ulmke, Mario Mietschke, and Klaus Bauckhage. Piezoelectric single nozzle droplet generator for production of monodisperse droplets of variable diameter. *Chemical engineering & technology*, 24(1):69–70, 2001.
- [27] Norbert Riefler and Thomas Wriedt. Generation of monodisperse micron-sized droplets using free adjustable signals. *Particle & Particle Systems Characterization*, 25(2):176–182, 2008.

- [28] Cecilie Gotaas, Pavel Havelka, Hugo A Jakobsen, and Hallvard F Svendsen. Evaluation of the impact parameter in droplet-droplet collision experiments by the aliasing method. *Physics of fluids*, 19(10):102105, 2007.
- [29] JJ Sangiovanni and M Labowsky. Burning times of linear fuel droplet arrays: a comparison of experiment and theory. *Combustion and flame*, 47:15–30, 1982.
- [30] AL Randolph and CK Law. Influence of physical mechanisms on soot formation and destruction in droplet burning. *Combustion and flame*, 64(3):267–284, 1986.
- [31] S Alam, A Nizami, and T Aziz. Fundamental aspects of droplet combustion modelling. *Intl Journal of Engineering Research and Applications*, 4(11):10–26, 2014.
- [32] N Nikolopoulos and G Bergeles. The effect of gas and liquid properties and droplet size ratio on the central collision between two unequal-size droplets in the reflexive regime. *International Journal of Heat and Mass Transfer*, 54(1):678–691, 2011.
- [33] Kannan N Premnath and John Abraham. Simulations of binary drop collisions with a multiple-relaxation-time lattice-boltzmann model. *Physics of Fluids*, 17(12):122105, 2005.